Terahertz oscillation in a noncollinear antiferromagnet under spin-orbit torques

De-Yun Zhao, Peng-Bin He,* and Meng-Qiu Cai
School of Physics and Electronics, Hunan University, Changsha 410082, China

(Received 4 October 2021; revised 6 December 2021; accepted 8 December 2021; published 15 December 2021)

We perform a theoretic study on equilibria and self-oscillations of a noncollinear antiferromagnet under spin-orbit torques and focus on the latter, which may be detected by the anormal Hall effect. Appealing to the 120° rotational symmetry, an analytically tractable single-vector equation is deduced from the complicated coupled Landau-Lifshitz-Gilbert equations. After defining the stable regions of all equilibria, we derive analytic formulas for the lower and upper thresholds of oscillation by Melnikov's method. We further reveal that the oscillation is largely pushed by the exchange interactions in the promise of an average balance between the dampinglike spin-orbit torque and the intrinsic damping. Its precessional conical angle and terahertz frequency can be adjusted by the current. We also analyze the oscillations numerically in the absence of 120° rotational symmetry for arbitrary spin polarizations and find similar results. This can be ascribed to the relatively weak anisotropy compared with the strong exchange.

DOI: 10.1103/PhysRevB.104.214423

I. INTRODUCTION

Antiferromagnets (AFMs) are promising for spintronics applications [1–3]. One of the advantages is the absence of a magnetic stray field, which can protect the devices from some detrimental magnetic perturbations. However, this results in the difficulty of controlling and detecting the antiferromagnetic states. As for the controlling, by introducing different spin torques generated by the magnons [4–6] and the spin(-polarized) currents [7], AFMs can be manipulated efficiently, such as the motion of domain walls [4–6,8–12], the switching [13–18], and the precession [19–22]. It is also worth noting that unequivocal detection of the collinear AFM states remains a challenge in experiments [18].

Thanks to the abundance of AFM materials, some noncollinear AFMs with a 120° spin structure, such as antiperovskite [23–30] and hexagonal [31–37] manganese compounds, exhibit large anomalous Hall conductivities, which can be used to differentiate various AFM states. Inspired by this favorable property, the current-driven dynamics of noncollinear AFM has started to attract some attention like its collinear counterpart, including the motion of domain walls [38–40], the switching [41–44], and the chiral-spin rotation [45]. As far as we know, the self-oscillation is seldom concerned, as simply mentioned in Refs. [41,44]. The experiment of Ref. [45] is about the spin orbit torque (SOT)-propelling rotation of total magnetization under the magnetic field. The self-oscillation is not only a typical nonlinear property of magnets but also the basis of magnetic oscillators. For noncollinear AFMs, the details of self-oscillation remain unexplored. So, it should be worth more effort in studying the thresholds, frequency, etc. of this oscillation.

Here, we will investigate the self-oscillation of noncollinear AFM under SOTs. To deal with this issue analytically, we first choose a current-injection scheme as shown in Fig. 1, which allows a 120° rotational symmetry and is of practical significance [46]. Phenomenologically, this model is described by three coupled Landau-Lifshitz-Gilbert (LLG) equations, which to treat analytically is very difficult. In Refs. [39,41], two Néel vectors and an average magnetization were introduced to reduce these complicated AFM equations and analyze the motion of domain walls and the switching. Alternatively, we will reduce the LLG equations to a single-vector equation according to the symmetry of the model.

Based on this reduced equation, we will analytically study the equilibria and self-oscillations. The stability of equilibria is analyzed by the linearization method. The self-oscillations are dealt with by Melnikov's method [47], which provides an analytic tool to study the limit circles for the perturbed dynamic systems with periodic trajectories. This method was applied on the self-oscillation of ferromagnets driven by spin-transfer torques by Serpico *et al.* and Bertotti *et al.* [48–51], and derived independently by Stiles and Miltat [52]. In this method, a self-oscillation is realized under the promise that external torques should balance the damping in average during a whole precession. To acquire this balance, different magnetic configurations and driven forces have been attempted [53–66]. For example, the balance can be achieved by tunable magnetic fields [53,57–61] or by a fieldlike spin torque [54–56], especially in the presence of thermal noise [62–66]. Recently, this method was also applied on the bipartite AFM to study the current-driven precession [67]. These studies present good agreement between the analytic calculation and the numeric simulation.

Up to now, Melnikov's method has mainly been applied on ferromagnetic (FM) systems, where the oscillation orbit is easily defined by the magnetic energy. For AFMs, more than one correlated orbit exists, corresponding to magnetic mo-

*hepengbin@hnu.edu.cn

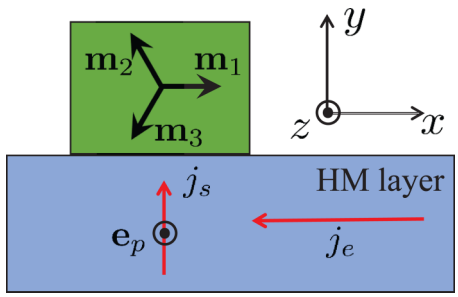

FIG. 1. Schematic diagram of the heavy-metal/antiferromagnet bilayer and coordinate system. $\mathbf{j}_e$ and $\mathbf{j}_s$ are the electric and spin currents, respectively. $\mathbf{e}_p$ denotes the direction of the spin polarization.

ments in different sublattices. Due to the exchange coupling, which transfers energy between different sublattices, the constant-energy trajectories are generally not well-defined. Therefore, it is difficult to apply Melnikov's method on AFM systems. However, for our model, by virtue of the 120° rotational symmetry, we get a reduced single-vector equation, which is analogous to a ferromagnetic one. Due to the strong exchange interaction, both the damping and the SOTs can be regarded as weak perturbations. So, Melnikov's method is applicable for dealing with the self-oscillation of this simplified structure analytically. In addition, for arbitrary spin-polarization directions, the oscillations will be analyzed numerically.

This paper is organized as follows. After the Introduction, Sec. I, and model description, Sec. II, the stable regions of all equilibria are analyzed in Sec. III. The oscillations are investigated in detail for the case with a spin polarization normal to the easy axes in Secs. IV and for arbitrary spin polarizations in Sec. V. Finally, we end with discussions in Sec. VI and conclusions in Sec. VII.

II. MODEL

We consider a noncollinear AFM thin film attached with a heavy metal (HM) layer, as shown in Fig. 1. With a longitudinal electric current flowing through the HM layer, the dampinglike and fieldlike SOTs are generated via the spin Hall effect or Rashba effect [7]. Under the SOTs, the magnetic dynamics in the AFM layer is governed by three coupled sublattice LLG equations,

$$\frac{d\mathbf{m}_i}{dt} = \mathbf{m}_i \times \frac{d\mathcal{E}}{d\mathbf{m}_i} + \alpha \mathbf{m}_i \times \frac{d\mathbf{m}_i}{dt} + \boldsymbol{\tau}_i, \tag{1}$$

where $\mathbf{m}_i$ are the unit vectors of magnetization in three sublattices marked by $i = 1, 2, 3$. α is the Gilbert constant of damping. Here, the inhomogeneous exchange contribution is ignored. So, we focus on the magnetic dynamics within the framework of a macrospin model, which is a reasonably good approximation for the small-size sample. Then, including the exchange and anisotropy terms, the reduced magnetic energy reads [39,44,46]

$$\mathcal{E} = \omega_{\rm ex} \sum_{i \neq j} \mathbf{m}_i \cdot \mathbf{m}_j - \omega_{\rm an} \sum_i \left(\mathbf{m}_i \cdot \mathbf{e}_a^i\right)^2, \tag{2}$$

where $\mathbf{e}_a^i$ are the unit vectors along the three easy axes and written as

$$\mathbf{e}_a^i = \cos\left[(i-1)\frac{2\pi}{3}\right]\mathbf{e}_x + \sin\left[(i-1)\frac{2\pi}{3}\right]\mathbf{e}_y. \tag{3}$$

The SOTs are expressed as

$$\boldsymbol{\tau}_i = -\omega_{\rm SOT}[\mathbf{m}_i \times (\mathbf{m}_i \times \mathbf{e}_z) + \beta \mathbf{m}_i \times \mathbf{e}_z], \tag{4}$$

with the spin polarization along the z axis and β denoting the relative strength of the fieldlike SOT compared with the dampinglike one. All parameters related with the strengths of the torques have been scaled with circular frequency. $\omega_{\rm ex} = \gamma J_0/(\mu_0 M_s)$ with γ being the gyromagnetic ratio, J_0 the intersublattice exchange constant, μ_0 the vacuum permeability, and M_s the saturation magnetization of each sublattice. $\omega_{\rm an} = \gamma K/(\mu_0 M_s)$, with K being the anisotropy constant. $\omega_{\rm SOT} = u/d$ with d being the thickness of AFM layer. u has the dimension of velocity, $u = \mu_B/(eM_s)\xi j_e$ with μ_B being the Bohr magneton, e the element charge, and j_e the electric current density. ξ is the SOT efficiency which equals $T_{\rm int}\theta_{\rm sH}$ [3,68,69], with $\theta_{\rm sH}$ being the spin Hall angle, and $T_{\rm int}$ the spin transparency of the interface [70].

To test our analytic results in the following sections, we will choose typical magnetic parameters of nonlinear AFM to do some numeric calculations. The magnetic parameters of Mn_3Sn [39] are adopted, which are listed as $J_0 = 1 \times 10^8\,\mathrm{J/m^3}$, $K = 1.6 \times 10^6\,\mathrm{J/m^3}$, $\mu_0 M_s = 1.26\,\mathrm{T}$. Then, $\omega_{\rm ex}/(2\pi) = 2.79\,\mathrm{THz}$ and $\omega_{\rm an}/(2\pi) = 44.67\,\mathrm{GHz}$. Other experimentally feasible parameters are taken as $d = 2\,\mathrm{nm}$, $\xi = 0.32$, $\beta = 0.1$, and $\alpha = 0.01$.

The system [Eqs. (1)–(4)] is invariant under the 120° rotation around z axis. So, it can be inferred that the solutions obey $m_{1z} = m_{2z} = m_{3z}$, and the included angle between the projections of $\mathbf{m}_{1,2,3}$ on the x-y plane is 120°. This can be verified by numerically integrating Eq. (1) for different magnetic states. In Figs. 2-4, we plot the evolutions of the components of $\mathbf{m}_{1,2,3}$ for the tilted AFM, precessional, and ferromagnetic states which all obey the 120° rotational symmetry around the z axis. According to this argument, the coupled LLG Eq. (1) can be reduced to a one-vector one. To realize this reduction, it is convenient to parametrize $\mathbf{m}_i$ in terms of the polar angles θ_i and the azimuthal ones ϕ_i according to $\mathbf{m}_i = (\sin\theta_i\cos\phi_i, \sin\theta_i\sin\phi_i, \cos\theta_i)$. Appealing to the symmetry, we can set $\theta_1 = \theta_2 = \theta_3 = \theta$, $\phi_1 = \phi$, $\phi_2 = \phi + 2\pi/3$, and $\phi_3 = \phi + 4\pi/3$ in spherical coordinates. Then, from Eq. (1), the reduced equations are derived as

$$\frac{d\theta}{dt} + \alpha \sin\theta \frac{d\phi}{dt} = -(\omega_{\rm an}\sin 2\phi + \omega_{\rm SOT})\sin\theta, \tag{5}$$

$$\alpha\frac{d\theta}{dt} - \sin\theta\frac{d\phi}{dt} = \left(\frac{3}{2}\omega_{\rm ex} + \omega_{\rm an}\cos^2\phi\right)\sin 2\theta - \beta\omega_{\rm SOT}\sin\theta. \tag{6}$$

A brief derivation of Eqs. (5) and (6) is presented in Appendix A. To apply Melnikov's method, it is necessary to rewrite Eqs. (5) and (6) in the Cartesian reference. By treating θ and ϕ as polar and azimuthal angles of a vector $\mathbf{n}$, i.e., defining $\mathbf{n} = (\sin\theta\cos\phi, \sin\theta\sin\phi, \cos\theta)$, Eqs. (5) and (6)

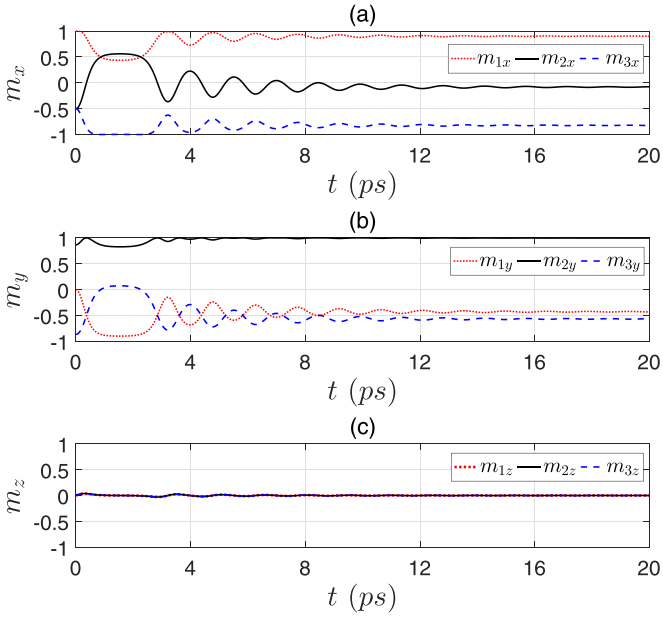

FIG. 2. Time evolutions of x components (a), y components (b), and z components (c) of $\mathbf{m}_{1,2,3}$ for the tilted AFM state. Here, the SOTs strength is taken as $\omega_{\rm SOT} = 0.7744\omega_{\rm an}$, just below the lower threshold of oscillation, corresponding to $j_e = 2.3531 \times 10^9 {\rm A/cm}^2$.

can be transformed as

$$\frac{d\mathbf{n}}{dt} = \mathbf{n} \times \frac{d\mathcal{E}_n}{d\mathbf{n}} + \alpha \mathbf{n} \times \frac{d\mathbf{n}}{dt} + \boldsymbol{\tau}_n, \tag{7}$$

where the reduced magnetic energy reads

$$\mathcal{E}_n = \frac{3}{2}\omega_{\rm ex}(\mathbf{n}\cdot\mathbf{e}_z)^2 - \omega_{\rm an}(\mathbf{n}\cdot\mathbf{e}_x)^2, \tag{8}$$

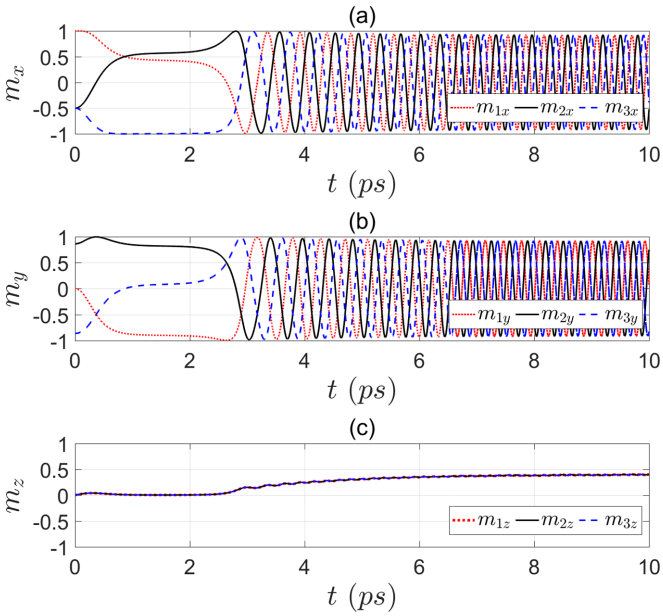

FIG. 3. Time evolutions of x components (a), y components (b), and z components (c) of $\mathbf{m}_{1,2,3}$ for the precession state. Here, the SOTs strength is taken as $\omega_{\rm SOT} = 0.7745\omega_{\rm an}$, just above the lower threshold of oscillation, corresponding to $j_e = 2.3534 \times 10^9 {\rm A/cm}^2$.

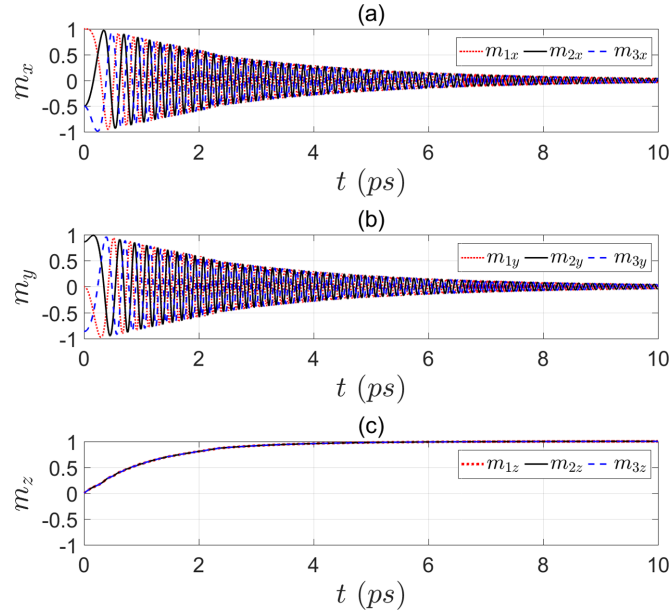

FIG. 4. Time evolutions of x components (a), y components (b), and z components (c) of $\mathbf{m}_{1,2,3}$ for the FM state. Here, the strength of SOTs $\omega_{\rm SOT} = 3\omega_{\rm an}$, above the upper threshold of oscillation, corresponding to $j_e = 9.1157 \times 10^9 {\rm A/cm}^2$.

and the SOTs are

$$\boldsymbol{\tau}_n = -\omega_{\rm SOT}[\mathbf{n} \times (\mathbf{n} \times \mathbf{e}_z) + \beta \mathbf{n} \times \mathbf{e}_z]. \tag{9}$$

It should be mentioned that $\mathbf{n}$ is not an order vector as in the bipartite AFM. In fact, $\mathbf{n} = \mathbf{m}_1$. Because the reduced Eq. (7) is formally different from Eq. (1) of $i = 1$, we use the symbol $\mathbf{n}$ to avoid confusion. According to the symmetry of our model, the dynamics of $\mathbf{m}_{1,2,3}$ can be represented by that of $\mathbf{n}$. From Eq. (8), it is easy to infer that the reduced system acts as a ferromagnetic film which possesses an easy axis along the x axis and an easy plane normal to the z axis. The easy-plane anisotropy is related to the exchange interaction between sublattices. Based on these reduced equations, we will study the equilibria and the dynamic states in the following sections.

III. EQUILIBRIA AND THEIR STABILITY

The stationary solutions can be calculated by taking $d\theta/dt = d\phi/dt = 0$ in Eqs. (5) and (6). It is apparent that $\sin\theta^0 = 0$ solves the equilibrium equations, corresponding to $\theta^0 = 0$ or π. For these two FM states, $\mathbf{m}_{1,2,3}$ go along the spin polarization $\mathbf{e}_p$ or the reverse, and all the torques are zero. The evolutions can be seen in Fig. 4 as an example.

By linear stability analysis (see Appendix B), the FM state $\theta^0 = 0$ is stable for $\omega_{\rm SOT} > \omega^u_{\rm SOT}$ while, for $\theta^0 = \pi$, the stable condition is $\omega_{\rm SOT} < -\omega^u_{\rm SOT}$, where

$$\omega^u_{\rm SOT} = \frac{\alpha}{1+\alpha\beta}(3\omega_{\rm ex} + \omega_{\rm an}). \tag{10}$$

For $\sin\theta^0 \neq 0$, the equilibrium equations become

$$\omega_{\rm an}\sin 2\phi^0 + \omega_{\rm SOT} = 0, \tag{11}$$

$$(3\omega_{\rm ex} + 2\omega_{\rm an}\cos^2\phi^0)\cos\theta^0 = \beta\omega_{\rm SOT}. \tag{12}$$

The solutions are expressed as

$$\phi^0 = \frac{1}{2}\left[(P-1)\pi + (-1)^P \arcsin\frac{\omega_{\rm SOT}}{\omega_{\rm an}}\right], \tag{13}$$

$$\theta^0 = \arccos\left[\frac{\beta\omega_{\rm SOT}}{3\omega_{\rm ex}+\omega_{\rm an}-(-1)^P\sqrt{\omega_{\rm an}^2-\omega_{\rm SOT}^2}}\right], \tag{14}$$

with $P = 1, 2, 3, 4$. For these solutions, the fieldlike SOT rotates $\mathbf{m}_{1,2,3}$ around the z axis. Then, the dampinglike SOT and the anisotropy torque tilt $\mathbf{m}_{1,2,3}$ away from the x-y plane. After achieving a balance among all the torques, $\mathbf{m}_{1,2,3}$ are at θ^0 with $\mathbf{e}_p$, and their projections on the x-y plane deviate from each easy axis as ϕ^0. For strong exchange interactions, θ^0 is small and $\mathbf{m}_{1,2,3}$ remain the AFM configuration roughly. So, it is referred to as tilted-AFM state. Its evolution is shown in Fig. 2. By linear stability analysis (see Appendix C), it can be inferred that the tilted-AFM state is stable for $P = 1, 3$ and $|\omega_{\rm SOT}| < \omega_{\rm an}$.

We have sought out all the stable equilibria. In the regions that $\omega_{\rm an} < \omega_{\rm SOT} < \omega_{\rm SOT}^u$, there is no stable equilibrium. In light of the Poincaré-Bendixson theorem [47,71], it can be argued that if none of the equilibrium points is stable in a two-dimensional dynamic system, there must exist precessional regimes [49]. Thus, a self-oscillation possibly emerges here. On the other hand, Figs. 2 and 3 reveal that the lower threshold of precession is about $0.7745\omega_{\rm an}$, smaller than $\omega_{\rm an}$. Hence, the details of oscillation cannot be foretold by the linear analysis. In view of the strong exchange interactions, the damping and the SOTs can be regarded as small perturbations. Then, the considered model is a weakly perturbed conservative system in which Melnikov's method [47,51,52] can be applied to analyze the self-oscillation.

IV. SELF-OSCILLATION

In this section, we will redefine the thresholds of self-oscillation and analyze the dependence of oscillation frequency on the SOTs by Melnikov's method.

A. Energy balance equation

The self-oscillation can be realized under an average balance between the energy supplied by the dampinglike SOT and the energy dissipated by the damping. So, it is necessary to calculate the rate of energy change. In Eq. (7), eliminating $d\mathbf{n}/dt$ from the damping term by iteration, and taking the cross product of this equation with $d\mathbf{n}/dt$, the rate of energy change can be expressed as

$$\frac{d\mathcal{E}_n}{dt} = \omega_T\left[(1+\alpha\beta)(\mathbf{n}\times\mathbf{e}_z)\cdot\frac{d\mathbf{n}}{dt} + (\beta-\alpha)\mathbf{e}_z\cdot\frac{d\mathbf{n}}{dt}\right] - \alpha\left(\mathbf{n}\times\frac{d\mathcal{E}_n}{d\mathbf{n}}\right)\cdot\frac{d\mathbf{n}}{dt}. \tag{15}$$

Since the energy $\mathcal{E}_n$ varies slowly for a self-oscillation, it is a good approximation to average $d\mathcal{E}_n/dt$ over a precession period. Then,

$$\oint_\Gamma \frac{d\mathcal{E}_n}{dt}dt = -\mathcal{W}_{\rm damp} + \mathcal{W}_{\rm SOT}, \tag{16}$$

where the work done by the SOTs during a whole precession reads

$$\mathcal{W}_{\rm SOT} = \omega_T\oint_\Gamma[(1+\alpha\beta)(\mathbf{n}\times\mathbf{e}_z) + (\beta-\alpha)\mathbf{e}_z]\cdot d\mathbf{n} \tag{17}$$

and the energy dissipated through the damping is

$$\mathcal{W}_{\rm damp} = \alpha\oint_\Gamma[3\omega_{\rm ex}(\mathbf{n}\cdot\mathbf{e}_z)(\mathbf{n}\times\mathbf{e}_z) - 2\omega_{\rm an}(\mathbf{n}\cdot\mathbf{e}_x)(\mathbf{n}\times\mathbf{e}_x)]\cdot d\mathbf{n}, \tag{18}$$

where we have used Eq. (8) to calculate $d\mathcal{E}_n/d\mathbf{n}$, and neglected the higher-order terms of α and $\omega_{\rm SOT}$. Due to the strong exchange interaction, the strengths of the SOTs and damping are sufficiently small, so both of them can be treated as perturbations. Therefore, the difference between the exact trajectory and the unperturbed one is also small. Accordingly, it is reasonable to take the integrals along a constant-energy trajectory determined by the exchange and anisotropy torques.

B. Constant-energy trajectories

Because $|\mathbf{n}| = 1$, the trail of the vector terminal of $\mathbf{n}$ locates on the surface of a unit sphere. So, the magnetization dynamics can be regarded as the motion of a point particle on a unit sphere. The constant-energy trajectories are given by the intersection of the unit sphere with the energy landscape Eq. (8) for various $\mathcal{E}_n$.

Three equilibria are defined by Eq. (8), according to which, the trajectories can be grouped into two types. The first equilibrium is that $\mathbf{n}$ points along the x axis. The corresponding minimal energy is $\mathcal{E}_{\rm min} = -\omega_{\rm an}$. The second one is a saddle point, for which $\mathbf{n}$ is along the y axis. The corresponding energy $\mathcal{E}_{\rm saddle} = 0$. The third one corresponds to state with maximal energy ($\mathcal{E}_{\rm max} = 3/2\omega_{\rm ex}$), with $\mathbf{n}$ oriented along the z axis.

As shown by the red dashed curves in Fig. 5(a), the two trajectories identified by $\mathcal{E}_{\rm saddle}$ are defined as the locus of the intersection of two planes (defined by $n_x = \pm\sqrt{3\omega_{\rm ex}/(2\omega_{\rm an})}n_z$) with the unit sphere. For a weak anisotropy ($\omega_{\rm an} \ll \omega_{\rm ex}$), these trajectories are very close to the x-y plane. These two trajectories divide the spherical surface into four regions.

In the two regions around the x axis, the low-energy trajectories are identified by $\mathcal{E}_{\rm min} < \mathcal{E}_n < \mathcal{E}_{\rm saddle}$. Here, $\mathbf{n}$ rotates around the x axis, as exemplified by the black dotted curves in Fig. 5(a). Obviously, the spin polarization $\mathbf{e}_p$ points outside of the trajectory. So, if projecting the dampinglike SOT on the direction of damping torque, its component is parallel to the damping torque in a half trajectory, whereas antiparallel in another half. Therefore, there cannot exist a balance between the dampinglike SOT and the damping during a whole precession [55,72]. And no self-oscillation emerges in these regions.

In the two regions around the z axis, the high-energy trajectories are identified by $\mathcal{E}_{\rm saddle} < \mathcal{E}_n < \mathcal{E}_{\rm max}$. Here, $\mathbf{n}$ rotates around the z axis, as exemplified by the blue solid curves in Fig. 5(a). Because the spin polarization is along the z axis, the dampinglike SOT is against the damping torque during the entire precession along these trajectories. Hence, a self-oscillation possibly emerges. To calculate the integrals

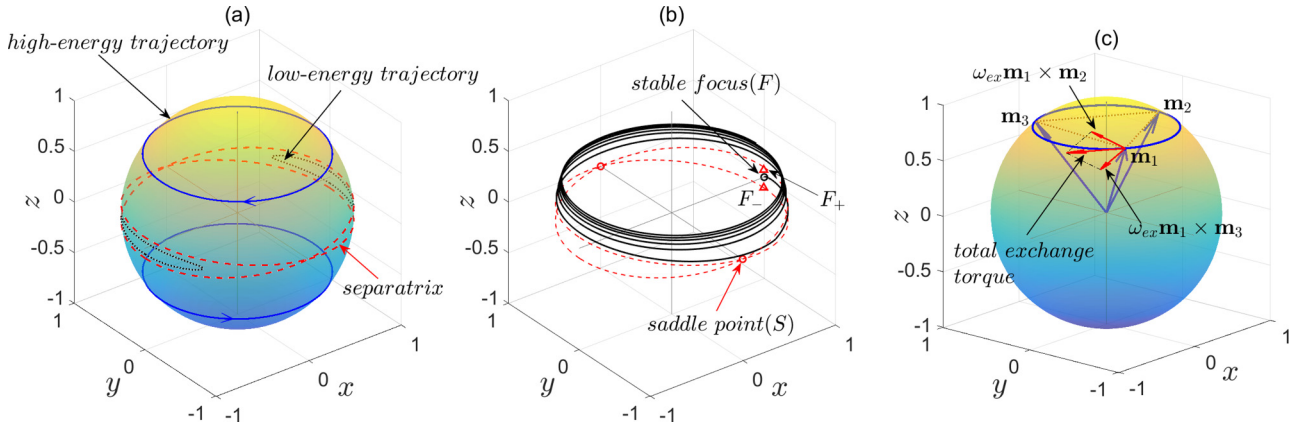

FIG. 5. (a) Examples of the constant-energy trajectories of $\mathbf{n}$ on the unit sphere. The dashed red curves are the separatrix corresponding to $\mathcal{E}_n = \mathcal{E}_{\text{saddle}}$. The dotted black curves are two low-energy trajectories around the easy axis, corresponding to $\mathcal{E}_n = -2/3\omega_{\text{an}}$. The solid blue curves are two high-energy trajectories around the spin polarization, corresponding to $\mathcal{E}_n = 1/2\omega_{\text{ex}}$. (b) Time-evolution trajectory of $\mathbf{m}_1(=\mathbf{n})$ at the lower threshold of precession with $\omega_{\text{SOT}} = 0.7745\omega_{\text{an}}$, corresponding to the evolutions of components in Fig. 3. $\mathbf{n}$ locates at the stable fucus initially. After about a quarter of a period, it shifts from the low-energy trajectory to the high-energy one near the saddle point. The points $F_\pm$ are in z-x plane and locate on the separatrix. (c) Schematic drawing of the trajectories and directions of precession for $\omega_{\text{SOT}} > 0$. The two exchange torques suffered by $\mathbf{m}_1$ are represented by the arrows at the endpoint of $\mathbf{m}_1$.

in Eq. (16), it is convenient to parametrize these high-energy trajectories as

$$n_x = a\cos\eta, \tag{19}$$

$$n_y = b\sin\eta, \tag{20}$$

where η varies from 0 to 2π, and

$$a = \sqrt{\frac{3\omega_{\text{ex}} - 2\mathcal{E}_n}{3\omega_{\text{ex}} + 2\omega_{\text{an}}}}, \tag{21}$$

$$b = \sqrt{\frac{3\omega_{\text{ex}} - 2\mathcal{E}_n}{3\omega_{\text{ex}}}}. \tag{22}$$

It should be emphasized that, for completeness, the fieldlike SOT is involved in the calculations, which is generally small in the spin-Hall-effect mechanism and dominant in the Rashba-effect mechanism [7]. The fieldlike SOT acts as an effective magnetic field along the spin-polarization direction. It can modify the constant-energy trajectories as the intersection of unit sphere with a hyperbolic cylindrical surface defined by

$$\frac{\left(n_z - \frac{\beta\omega_{\text{SOT}}}{2\omega_{\text{ex}}}\right)^2}{a_z^2} - \frac{n_x^2}{a_x^2} = 1, \tag{23}$$

where $a_z = \sqrt{[2\mathcal{E}_n + (\beta\omega_{\text{SOT}})^2/(3\omega_{\text{ex}})]/(3\omega_{\text{ex}})}$ and $a_x = \sqrt{[2\mathcal{E}_n + (\beta\omega_{\text{SOT}})^2/(3\omega_{\text{ex}})]/(2\omega_{\text{an}})}$. For an experimentally feasible parameter range, $\beta\omega_{\text{SOT}} \ll \omega_{\text{ex}}$. So, the modification of the trajectory is very small. It is a reasonable approximation to complete the integrals [such as Eqs. (17), (18), and (29)] along the constant-energy trajectories [Eq. (8)], not taking into account the fieldlike SOT. This point can be verified by the numeric results, for example, Fig. 6.

C. Balance between dampinglike SOT and damping

By use of the parameterized high-energy trajectories described by Eqs. (19)–(22), the supplied energy Eq. (17) and the dissipated energy Eq. (18) can be calculated analytically, which read

$$\mathcal{W}_{\text{SOT}} = 2\pi\frac{3\omega_{\text{ex}} - 2\mathcal{E}_n}{\sqrt{3\omega_{\text{ex}}(3\omega_{\text{ex}} + 2\omega_{\text{an}})}}(1 + \alpha\beta)\omega_{\text{SOT}} \tag{24}$$

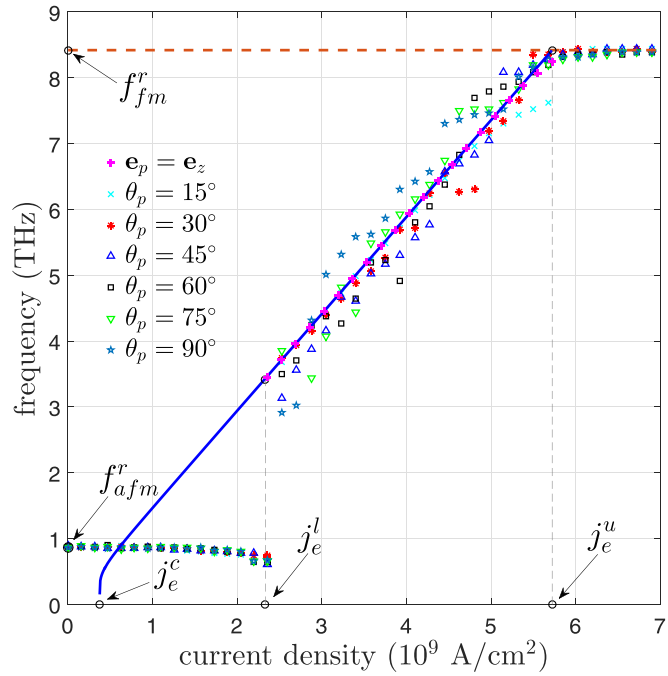

FIG. 6. Oscillation frequency versus current density. Symbols are simulation results for different spin-polarization directions with $\mathbf{e}_p = (0, \sin\theta_p, \cos\theta_p)$. The solid line is plotted from analytic expressions Eqs. (27) and (35). The upper (lower) threshold current $j_e^{u(l)} = edM_s/(\xi\mu_B)\omega_{\text{SOT}}^{u(l)}$, and $j_e^c = edM_s/(\xi\mu_B)\omega_{\text{SOT}}^c$. ω_{SOT}^u, ω_{SOT}^l, and ω_{SOT}^c are defined by Eqs. (10), (30), and (28), respectively.

and

$$\mathcal{W}_{\text{damp}} = 8\alpha\sqrt{\frac{\omega_{\text{an}}+\mathcal{E}_n}{6\omega_{\text{ex}}}}[3\omega_{\text{ex}}E(k) - 2\mathcal{E}_n K(k)], \quad (25)$$

where E and K denote the complete elliptic integral of the second and first kinds, and the modulus

$$k = \frac{\omega_{\text{an}}(3\omega_{\text{ex}} - 2\mathcal{E}_n)}{3\omega_{\text{ex}}(\omega_{\text{an}} + \mathcal{E}_n)}. \quad (26)$$

For a self-oscillation, the dampinglike SOT balances the damping in average during a whole period, so $\oint_\Gamma (d\mathcal{E}_n/dt)dt = 0$. Then, to excite a self-oscillation on a constant-energy trajectory marked by $\mathcal{E}_n$, the SOT strength

$$\omega_{\text{SOT}} = \frac{2}{\pi}\frac{\alpha}{1+\alpha\beta}\frac{\sqrt{2(\omega_{\text{an}}+\mathcal{E}_n)(3\omega_{\text{ex}}+2\omega_{\text{an}})}}{3\omega_{\text{ex}} - 2\mathcal{E}_n} \times[3\omega_{\text{ex}}E(k) - 2\mathcal{E}_n K(k)]. \quad (27)$$

When $\mathcal{E}_n$ approaches $\mathcal{E}_{\max}$, the upper threshold for self-oscillation can be obtained from Eq. (27), which is just the critical value ω^u_{SOT} [Eq. (10)] for the onset of the FM state. This is consistent with the linear stability analysis of the FM state. Taking another limit that $\mathcal{E}_n$ approaches $\mathcal{E}_{\text{saddle}}$, a lower threshold can be had:

$$\omega^c_{\text{SOT}} = \frac{2}{\pi}\frac{\alpha}{1+\alpha\beta}\sqrt{2(3\omega_{\text{ex}}+2\omega_{\text{an}})\omega_{\text{an}}}. \quad (28)$$

By the used parameters, the lower threshold Eq. (28) is $0.1238\omega_{\text{an}}$, which is smaller than the numerical value $0.7745\omega_{\text{an}}$, as displayed in Figs. 2 and 3. This result means that, in the crossover from the tilted AFM state to the self-oscillation, neither the linearization method nor the Melnikov method fails to predict the critical value of SOTs.

D. Lower threshold of self-oscillation

To get an analytic expression of the lower threshold, a method developed by Taniguchi *et al.* [57] is very useful, which has provided an analytic result consistent with the numerical calculation very well for the ferromagnetic case. This method involves the energy cost with the magnetization evolving from the fucus to the high-energy trajectory. Figure 5(b) shows the evolution trajectory of $\mathbf{m}_1(=\mathbf{n})$ at the lower threshold $\omega_{\text{SOT}} = 0.7745\omega_{\text{an}}$. $\mathbf{m}_1$ is initialized along the positive x direction (point F on the sphere). Before precessing along the high-energy trajectory, $\mathbf{m}_1$ must evolve from the initial stable state (F) to the saddle point (S) in the low-energy region. The energy of this trajectory is not constant. Hence, $\mathbf{m}_1$ needs to surmount an energy barrier $\mathcal{E}_{\text{saddle}} - \mathcal{E}_{\min} = \omega_{\text{an}}$ before getting to the saddle point, namely, in the process from the stationary initial state to the self-oscillation, apart from balancing the damping torque, the SOT should also do work to conquer the barrier. This work-energy relation reads

$$\omega_{\text{SOT}}\int_F^S [(1+\alpha\beta)(\mathbf{n}\times\mathbf{e}_z) + (\beta-\alpha)\mathbf{e}_z]\cdot d\mathbf{n} = \alpha\int_F^S [3\omega_{\text{ex}}(\mathbf{n}\times\mathbf{e}_z)(\mathbf{n}\times\mathbf{e}_z) - 2\omega_{\text{an}}(\mathbf{n}\times\mathbf{e}_x)(\mathbf{n}\times\mathbf{e}_x)]\cdot d\mathbf{n} + \omega_{\text{an}}. \quad (29)$$

In the absence of an explicit expression for the trajectory, it is impossible to complete the integrals analytically. However, owing to $\omega_{\text{an}} \ll \omega_{\text{ex}}$, the trajectory of $\mathcal{E}_{\text{saddle}}$ is tightly close to the x-y plane. As shown in Fig. 5(b), the points $F_\pm$ are very near to the fucus F. $F_\pm$ situate in the z-x plane, with $n_z = \pm\sqrt{2\omega_{\text{an}}/(3\omega_{\text{ex}}+2\omega_{\text{an}})}$ and $n_x = \sqrt{3\omega_{\text{ex}}/(3\omega_{ex}+2\omega_{\text{an}})}$. Therefore, the integral trajectory can be approximately replaced by the constant-energy one of $\mathcal{E}_{\text{saddle}}$ from $F_\pm$ to S. Then, by integrating Eq. (29), a lower threshold of oscillation is derived:

$$\omega^l_{\text{SOT}} = \frac{\left(\alpha\sqrt{6\omega_{\text{ex}}\omega_{\text{an}}} + \omega_{\text{an}}\right)\sqrt{3\omega_{\text{ex}}+2\omega_{\text{an}}}}{\frac{\pi}{2}(1+\alpha\beta)\sqrt{3\omega_{\text{ex}}} + (\alpha-\beta)\sqrt{2\omega_{\text{an}}}}. \quad (30)$$

Taking the used parameters, $\omega^l_{\text{SOT}} \approx 0.7677\omega_{\text{an}}$, which is very close to the value estimated from the numerical simulation.

E. Frequency

For the self-oscillation, The dampinglike SOT and the damping torque should cancel each other on average during a precession. So, the precession is mainly propelled by the exchange torque and the anisotropy one. The period T, which relates to the frequency via $f = 1/T$, is determined by the unperturbed parts of Eq. (7), which are written in the Cartesian coordinate system as

$$\frac{dn_x}{dt} = 3\omega_{\text{ex}}n_y n_z, \quad (31)$$

$$\frac{dn_y}{dt} = -(3\omega_{\text{ex}}+2\omega_{\text{an}})n_z n_x, \quad (32)$$

$$\frac{dn_z}{dt} = 2\omega_{\text{an}}n_x n_y. \quad (33)$$

Substituting Eqs. (19) and (20) into one of above equations and integrating over the whole trajectory, the period can be calculated as a function of $\mathcal{E}_n$:

$$T = \frac{1}{3\omega_{\text{ex}}}\frac{a}{b}\int_0^{2\pi}\frac{d\eta}{\sqrt{1-a^2\cos^2\eta - b^2\sin^2\eta}}. \quad (34)$$

Accomplishing the integral and using Eqs. (21) and (22), the final result is expressed by the elliptical integral,

$$f = \frac{1}{4}\frac{\sqrt{6\omega_{\text{ex}}(\omega_{\text{an}}+\mathcal{E}_n)}}{K(k)}, \quad (35)$$

where K denotes the complete elliptic integral of the first kind, the modulus k is still Eq. (26). When $\mathcal{E}_n = \mathcal{E}_{\text{saddle}}$, $f = 0$. When $\mathcal{E}_n = \mathcal{E}_{\max}$, $f = 1/(2\pi)\sqrt{3\omega_{\text{ex}}(3\omega_{\text{ex}}+2\omega_{\text{an}})}$, which is just the resonance frequency of FM states.

$\mathcal{W}_{\text{SOT}}$, $\mathcal{W}_{\text{damp}}$, and f are functions of the energy $\mathcal{E}_n$, corresponding to a self-oscillation state. Eliminating $\mathcal{E}_n$ from Eqs. (27) and (35), one can obtain the relation between the frequency and ω_{SOT}. Although there is no explicit analytic expression, the f-j_e relation is shown by the solid line in Fig. 6. The numeric result is also shown by the symbol + in Fig. 6,

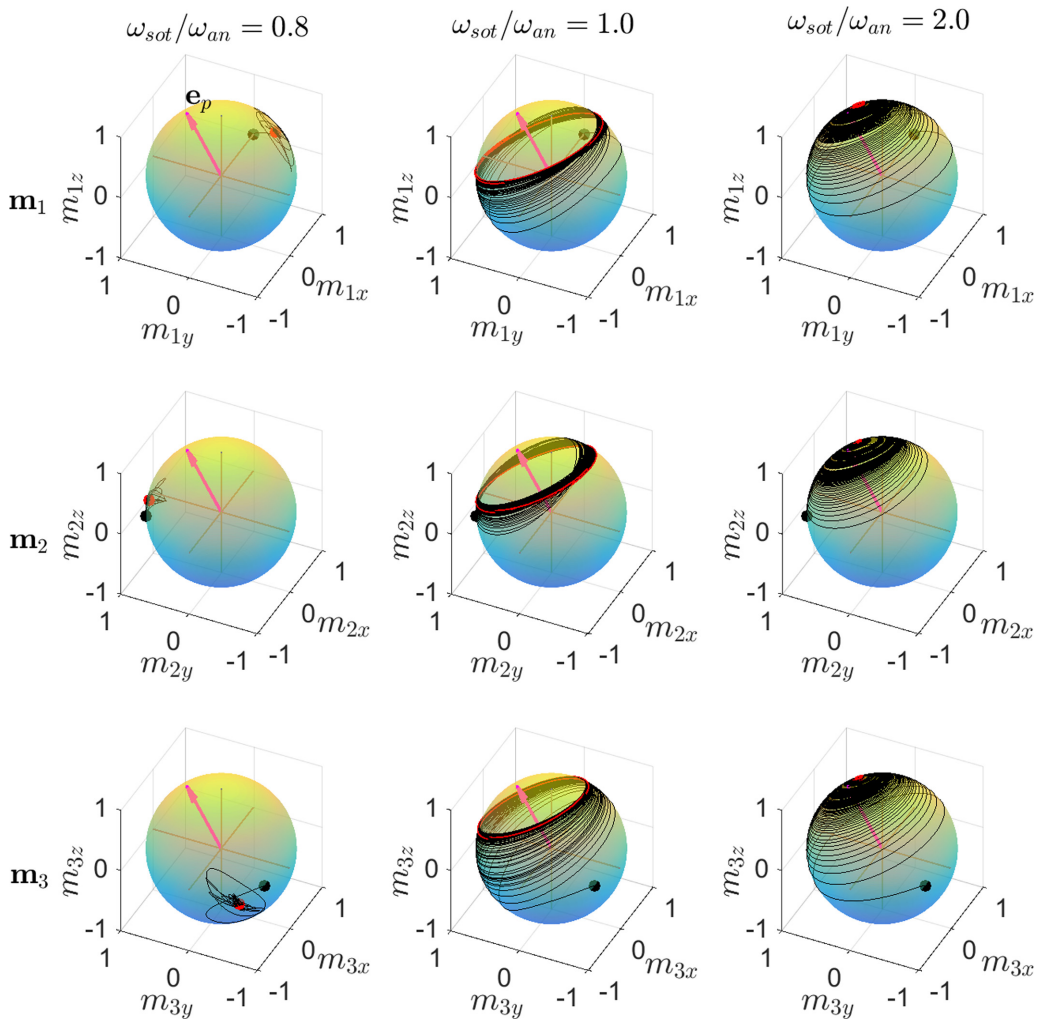

FIG. 7. Evolutions of $\mathbf{m}_1$ (the first row), $\mathbf{m}_2$ (the second row), and $\mathbf{m}_3$ (the third row) for $\omega_{\rm SOT} = 0.8\omega_{\rm an}$ (the first column), $\omega_{\rm SOT} = \omega_{\rm an}$ (the second column), and $\omega_{\rm SOT} = 2\omega_{\rm an}$ (the third column). The red arrow denotes the spin-polarization direction that $\mathbf{e}_p = (0, 1/2, \sqrt{3}/2)$. The black dots represent the initial states without SOTs. The red curves are the final orbits of evolution, and the red dots represent the final states of fixed points.

very consistent with the analytic calculations. Obviously, the frequency increases almost linearly with $\omega_{\rm SOT}$.

V. ARBITRARY SPIN POLARIZATION

In the previous sections, to illustrate the current-driven magnetization oscillation in noncollinear AFM with 120° rotation symmetry, we have considered SOTs with spin polarization perpendicular to the easy axes of three sublattices, which keeps the static symmetry and allows for strictly analytic calculations.

Recently, it has been reported [73,74] that the spin polarization can be modified to deviate from the usual direction $\mathbf{j}_e \times \mathbf{n}$ with $\mathbf{n}$ being the interface normal. In this case, the 120° rotation symmetry is destroyed and a simple analytic calculation is impossible. So, we could only analyze the oscillation numerically. By integrating the coupled LLG equations [Eq. (1)], we can obtain the evolutions of $\mathbf{m}_{1,2,3}$. As an example, Fig. 7 summarizes three typical evolutions, including the tilted AFM, precessional, and FM states for $\mathbf{e}_p = (0, 1/2, \sqrt{3}/2)$. Without SOTs, $\mathbf{m}_{1,2,3}$ are along the three easy axes. The anisotropy torques are zero, and the exchange torques cancel each other. The system is in a strict nonlinear AFM state. Applying small SOTs, $\mathbf{m}_{1,2,3}$ deviate from each easy axis. Up to a lower threshold, a static state (tilted AFM) remains under a delicate balance between the exchange torques, the anisotropy torques, and the SOTs, as shown in the first column of Fig. 7. When the current exceeds a lower threshold, breaking of the balance results in a nonlinear precession around the spin-polarization direction, as shown in the second column of Fig. 7. Further increasing the current, the cone angle of precession decreases and the orbit on the sphere surface shrinks to a point, as shown in the third column of Fig. 7. Under high currents, $\mathbf{m}_{1,2,3}$ point in the same direction, determined by the equilibrium of the SOTs and the anisotropy torque. This behaviors are qualitatively similar to the case that $\mathbf{e}_p = \mathbf{e}_z$.

Moreover, we extract the values of frequency from the evolution curves for different spin polarizations and currents, and illustrate the dependence of frequency on the current density in Fig. 6. We find that tilting the spin polarization influences the frequency of oscillation slightly. Although the frequencies

deviate from the values (the solid line in Fig. 6) of $\mathbf{e}_p = \mathbf{e}_z$, the deviations are small and the linear trend of frequency versus current is nearly unchanged. In addition, the lower and upper thresholds are almost unchanged. These small differences for different spin polarizations are largely due to the smallness of anisotropy. The frequencies of both the linear and nonlinear oscillations are to a great extent determined by the exchange interaction, namely, it is mainly the exchange torques between $\mathbf{m}_{1,2,3}$ to propel the precessions. The SOTs balance the damping torque, keeping a stable precession.

Below the lower threshold, there exists a linear oscillating mode with its frequency near the resonance frequency (shown by the lower circle on the f axis of Fig. 6) of the AFM state with $\mathbf{m}_{1,2,3}$ along each easy axis [$\mathbf{e}_a^{1,2,3}$ that is defined by Eq. (3)]. Without regard to the damping and SOTs, and linearizing Eq. (1) around $\mathbf{m}_{1,2,3} = \mathbf{e}_a^{1,2,3}$, this frequency is derived as $f_{\mathrm{AFM}}^r = 1/(2\pi)\sqrt{2\omega_{\mathrm{an}}(2\omega_{\mathrm{an}} + 3\omega_{\mathrm{ex}})}$. Beyond the upper threshold, there exists another linear oscillating mode with its frequency approaching the resonance frequency (shown by the upper circle on the f axis) of FM state with $\mathbf{m}_{1,2,3}$ along $\mathbf{e}_z$. By linearizing Eq. (1) around $\mathbf{m}_{1,2,3} = \mathbf{e}_z$, this frequency is obtained as $f_{\mathrm{FM}}^r = 1/(2\pi)\sqrt{3\omega_{\mathrm{ex}}(3\omega_{\mathrm{ex}} + 2\omega_{\mathrm{an}})}$.

In Fig. 6, it is also observed that there is a discontinuity in the frequency when the current crosses the lower threshold. This can be ascribed to the shift in the oscillation state from the low-energy trajectory (around the easy axis) to the high-energy one (around the spin-polarization direction). In contrast, on both sides of the upper threshold, the nonlinear (below the upper threshold) and linear (beyond the upper threshold) oscillations are all around the spin-polarization direction. So, there is no discontinuity of frequency.

VI. DISCUSSION

First, of particular note is that we adopt a three-sublattice macrospin model which assumes a uniform distribution of the magnetization for each sublattice, implying a periodic boundary condition. In the surface or edge of the AFM film, the exchange energy is generally decreased due to low coordination. A possible absence of compensation results in nonzero static surface magnetization. Likewise, the anisotropy and damping at surface are different from their bulk counterparts. Due to these differences between the surface and bulk, the magnetization precession is not coherent. A surface oscillation mode should be introduced, with different frequencies and strengths from the bulk oscillation. In a simplified picture, it is reasonable to disentangle these two kinds of modes. As a general trend, it can be speculated that a weak surface signal maybe emerges near the bulk peak in the frequency spectrum for different currents. On the other hand, the strong exchange can narrow the range of nonuniform magnetization. Then, combining with shrinking device sizes, the deviations from the prediction of macrospin model can be suppressed. Furthermore, the anomalous Hall effect is sensitive to the bulk magnetic behaviors [75]. Consequently, the macrospin model may be used to give a basic understanding of the self-oscillation. In the absence of more detailed knowledge of the surface, we currently do not establish a suitable model to describe the surface magnetic dynamics of noncollinear AFMs. We hope our results based on the macrospin assumption can act as a starting point for future in-depth analyses.

Second, the self-oscillation is mainly propelled by the exchange interaction. As shown by Fig. 5(c), the magnetic moment in one sublattice bears two exchange torques from the other two sublattices. The total torques drive this moment rotating around the spin-polarization direction under the left-hand screw rule. Here, the torques from the anisotropy field and the fieldlike SOT also contribute to the precession. But, due to $\omega_{\mathrm{ex}} \gg \omega_{\mathrm{an}}$ and $\omega_{\mathrm{ex}} \gg \beta\omega_{\mathrm{SOT}}$, the exchange torques are dominant for propelling the self-oscillation. This is also the reason why the frequencies are very close for different spin polarizations.

Third, the analytic and numeric results reveal that $\mathbf{m}_{1,2,3}$ precess stably on a conical surface for the strong exchange. The cone angle of precession decreases with ω_{SOT} increasing. This is ascribed to the balance between the dampinglike SOT and the intrinsic damping torque. According to the direction of procession [shown by Fig. 5(c)], the damping torque turns $\mathbf{m}_{1,2,3}$ away from the rotational axis (z axis). Meanwhile, the dampinglike SOT turns $\mathbf{m}_{1,2,3}$ close to the rotational axis. When increasing the SOT, to keep this balance, the precessional angle decreases. When $\omega_{\mathrm{SOT}} = \omega_{\mathrm{SOT}}^u$, the precessional angle becomes zero and the self-oscillation disappears. Reference [41] studied a simplified case, in which $\mathbf{m}_{1,2,3}$ remain in one plane during the precession. This corresponds to the self-oscillation near the lower threshold in our paper.

Fourth, the values of thresholds are an interesting issue for future experiments. The threshold currents ($\sim 10^9 \mathrm{A/cm}^2$) in Fig. 6 are a little high from the application point of view. To decrease the current sustaining the self-oscillation, one can choose some materials with small damping, as indicated by Eqs. (10) and (30). Furthermore, considering $\omega_{\mathrm{SOT}} = \mu_B/(eM_s)\xi j_e/d$, a large SOT efficiency ($\xi \propto \theta_{\mathrm{sH}}$) or a large spin Hall angle (as summarized in Ref. [76]) can also reduce the current.

Finally, at the present time we are not aware of any experimental studies concerning nonlinear precessions of magnetization in the noncollinear AFMs. However, the strong anisotropic anomalous Hall effect and spin Hall effect [24,29,35] can be used to test our theoretical predictions. In these works [24,29,35], it was revealed that the intrinsic Hall conductivity periodically depends on the in-plane magnetization direction. It has been argued that the spin-torque switching of the noncollinear AFM order can be detected by the anomalous Hall effect [44]. Here, for a certain current, the SOT-driving precession of in-plane (x-y plane) magnetization may result in an oscillation of the Hall conductivity. Additionally, the nonzero total magnetization along the spin polarization $\mathbf{e}_p$ contributes a constant anomalous Hall conductivity. Therefore, setting a fixed Hall bar and applying the SOTs, a periodic oscillation of the Hall conductivity is expected to be observed, in analogy with the oscillation of magnetic resistance for a ferromagnetic precession.

VII. SUMMARY

In this paper, we systematically investigate the equilibria and the self-oscillations in a noncollinear AFM driven by

the SOTs. According to the 120° rotational symmetry, we reduce the three coupled LLG equations to a single-vector equation. By the linear stability analysis, we seek out all the stable equilibria. We focus on the self-oscillation which emerges in the region without any stable equilibrium. Utilizing Melnikov's method, we deduce the analytic formulas of the lower and upper thresholds of oscillation, as well as the oscillation frequency. We find that the frequency locates in the terahertz range and increases almost linearly with the current. Furthermore, the roles of different torques are illustrated: the dampinglike SOT counteracts the intrinsic damping to sustain a stable precession; the exchange and anisotropy torques, and the fieldlike SOT propel the precession with the exchange playing a major role. For arbitrary spin polarization, we obtain qualitatively similar results as the case of $\mathbf{e}_p = \mathbf{e}_z$ by numeric calculations. This is attributed to the small ratio of the anisotropy to the exchange. Given that the noncollinear AFM auto-oscillator driven by the SOTs has not been investigated, our paper may provide a way to achieve THz oscillation in nanoscale AFM devices.

ACKNOWLEDGMENTS

This work was supported by the National Natural Science Foundation of China (Grants No. 51972103 and No. 21938002).

APPENDIX A: DERIVATIONS OF EQS. (5) AND (6)

It is convenient to adopt the spherical coordinates to analyze the symmetry and reduce the coupled LLG equations according to this symmetry. First, we parametrize $\mathbf{m}_i$ in terms of the polar angles θ_i and the azimuthal ones ϕ_i according to $\mathbf{m}_i = (\sin\theta_i\cos\phi_i, \sin\theta_i\sin\phi_i, \cos\theta_i)$. Then, the coupled LLG equations [Eqs (1)–(4)] can be written explicitly as

$$\frac{d\theta_1}{dt} + \alpha\sin\theta_1\frac{d\phi_1}{dt} = \omega_{\rm ex}[\sin\theta_2\sin(\phi_1-\phi_2) + \sin\theta_3\sin(\phi_1-\phi_3)] - \{\omega_{\rm an}\sin[2(\phi_1-\Phi_1)] + \omega_{\rm SOT}\}\sin\theta_1, \tag{A1}$$

$$-\alpha\frac{d\theta_1}{dt} + \sin\theta_1\frac{d\phi_1}{dt} = \omega_{\rm ex}\{-\sin\theta_1(\cos\theta_2+\cos\theta_3) + \cos\theta_1[\sin\theta_2\cos(\phi_1-\phi_2) + \sin\theta_3\cos(\phi_1-\phi_3)]\} - \omega_{\rm an}\sin 2\theta_1\cos^2(\phi_1-\Phi_1) + \beta\omega_{\rm SOT}\sin\theta_1, \tag{A2}$$

$$\frac{d\theta_2}{dt} + \alpha\sin\theta_2\frac{d\phi_2}{dt} = \omega_{\rm ex}[\sin\theta_3\sin(\phi_2-\phi_3) + \sin\theta_1\sin(\phi_2-\phi_1)] - \{\omega_{\rm an}\sin[2(\phi_2-\Phi_2)] + \omega_{\rm SOT}\}\sin\theta_2, \tag{A3}$$

$$-\alpha\frac{d\theta_2}{dt} + \sin\theta_2\frac{d\phi_2}{dt} = \omega_{\rm ex}\{-\sin\theta_2(\cos\theta_3+\cos\theta_1) + \cos\theta_2[\sin\theta_3\cos(\phi_2-\phi_3) + \sin\theta_1\cos(\phi_2-\phi_1)]\} - \omega_{\rm an}\sin 2\theta_2\cos^2(\phi_2-\Phi_2) + \beta\omega_{\rm SOT}\sin\theta_2, \tag{A4}$$

$$\frac{d\theta_3}{dt} + \alpha\sin\theta_3\frac{d\phi_3}{dt} = \omega_{\rm ex}[\sin\theta_1\sin(\phi_3-\phi_1) + \sin\theta_2\sin(\phi_3-\phi_2)] - \{\omega_{\rm an}\sin[2(\phi_3-\Phi_3)] + \omega_{\rm SOT}\}\sin\theta_3, \tag{A5}$$

$$-\alpha\frac{d\theta_3}{dt} + \sin\theta_3\frac{d\phi_3}{dt} = \omega_{\rm ex}\{-\sin\theta_3(\cos\theta_1+\cos\theta_2) + \cos\theta_3[\sin\theta_1\cos(\phi_3-\phi_1) + \sin\theta_2\cos(\phi_3-\phi_2)]\} - \omega_{\rm an}\sin 2\theta_3\cos^2(\phi_3-\Phi_3) + \beta\omega_{\rm SOT}\sin\theta_3, \tag{A6}$$

where $\Phi_1 = 0$, $\Phi_2 = 2\pi/3$, and $\Phi_3 = 4\pi/3$ are the angles included between the anisotropy directions and the x axis. Appealing to the symmetry, we can set $\theta_1 = \theta_2 = \theta_3 = \theta$, $\phi_1 = \phi$, $\phi_2 = \phi + 2\pi/3$, and $\phi_3 = \phi + 4\pi/3$. Then, from the above equations, the reduced equations [Eqs. (5) and (6)] are derived.

APPENDIX B: STABILITY ANALYSIS OF FM STATES

In this and the next Appendix, the linear stability analysis is performed on the equilibria derived in Sec. III, including FM and tilted AFM states.

For the FM states, $\mathbf{m}_i$ are along the z axis and ϕ is not defined. To avoid working with equilibria near the singular points of the spherical coordinate system, we use Eqs. (7)–(9) instead. Then, corresponding to $\theta^0 = 0$ and π, $\mathbf{n}_0 = \pm\mathbf{e}_z$. To take stability analysis, we linearize Eq. (7) by assuming $\mathbf{n} = \mathbf{n}_0 + \delta n_x\mathbf{e}_x + \delta n_y\mathbf{e}_y$, with δn_x and δn_y being the responses to a small perturbation. Inserting the oscillating solutions ($\delta n_x, \delta n_y \propto e^{\lambda t}$) into the linearized equations, one can obtain the secular equation,

$$(1+\alpha^2)\lambda^2 + a_1\lambda + a_2 = 0, \tag{B1}$$

where

$$a_1 = \pm 2(1+\alpha\beta)\omega_{\rm SOT} - 2\alpha(3\omega_{\rm ex} + \omega_{\rm an}), \tag{B2}$$

$$a_2 = \frac{1}{(1+\beta^2)}\{[3\omega_{\rm ex}(3\omega_{\rm ex}+2\omega_{\rm an}) - \beta^2\omega_{\rm an}^2] + [(1+\beta^2)\omega_{\rm SOT} \mp \beta(3\omega_{\rm ex}+\omega_{\rm an})]^2\}. \tag{B3}$$

According to the Routh-Hurwitz Criterion [77–79], if a_1 and a_2 are all positive, the real parts of all roots of λ are negative so the equilibrium is stable. For typical experiments, $\alpha \sim 0.01$, $\beta \lesssim 1$, $\omega_{\rm ex} \gg \omega_{\rm an}$, and $\omega_{\rm ex} \gg \omega_{\rm SOT}$. So, we can estimate that $a_2 > 0$. From $a_1 > 0$, one can obtain that, for $\mathbf{n}_0 = 1$, $\omega_{\rm SOT} > \omega_{\rm SOT}^u$. While, for $\mathbf{n}_0 = -1$, $\omega_{\rm SOT} < -\omega_{\rm SOT}^u$, where

$$\omega_{\rm SOT}^u = \frac{\alpha}{1+\alpha\beta}(3\omega_{\rm ex} + \omega_{\rm an}). \tag{B4}$$

APPENDIX C: STABILITY ANALYSIS OF TILTED AFM STATES

For this kind of state, it is convenient to analyze their stability in the spherical coordinate system. We assume $\theta = \theta^0 + \theta'$, and $\phi^0 = \phi^0 + \phi'$, with θ' and ϕ' being the responses to a small perturbation. Inserting this ansatz into Eqs. (5) and (6) and keeping linear terms of θ' and ϕ', we have

$$\begin{pmatrix} 1 & \alpha \sin\theta^0 \\ -\alpha & \sin\theta^0 \end{pmatrix} \frac{d}{dt} \begin{pmatrix} \theta' \\ \phi' \end{pmatrix} = \begin{pmatrix} a_{11} & a_{12} \\ a_{21} & a_{22} \end{pmatrix} \begin{pmatrix} \theta' \\ \phi' \end{pmatrix}, \quad \text{(C1)}$$

where the matrix elements read $a_{11} = 0$, $a_{12} = -2\omega_{\rm an} \sin\theta^0 \cos 2\phi^0$, $a_{21} = \beta\omega_{\rm SOT} \sin\theta^0 \tan\theta^0$, and $a_{22} = -\omega_{\rm SOT} \sin 2\theta^0$. These parameters have been simplified by use of the equilibrium Eqs. (11) and (12). Usually, the solutions of Eq. (C1) take the form $(\theta', \phi') \propto e^{\lambda t}$. To ensure the existence of nontrivial solutions, λ satisfies the secular equation:

$$\begin{vmatrix} \lambda - a_{11} & \lambda\alpha \sin\theta^0 - a_{12} \\ -\alpha\lambda - a_{21} & \lambda \sin\theta^0 - a_{22} \end{vmatrix} = 0. \quad \text{(C2)}$$

Inserting Eqs. (13) and (14) into Eq. (C2), the secular equation as Eq. (B1) can be derived. For $P = 1$ and 3, the parameters

$$a_1 = A\frac{2 - \alpha\beta}{\beta}(3\omega_{\rm ex} + \omega_{\rm an} - B) + \alpha(3\omega_{\rm ex} + \omega_{\rm an} + 3B), \quad \text{(C3)}$$

$$a_2 = 2B[(3\omega_{\rm ex} + \omega_{\rm an})(1 - A) + (1 + A)B], \quad \text{(C4)}$$

where

$$A = \frac{\beta^2\omega_{\rm SOT}^2}{3\omega_{\rm ex}(3\omega_{\rm ex} + 2\omega_{\rm an}) + \omega_{\rm SOT}^2}, \quad \text{(C5)}$$

$$B = \sqrt{\omega_{\rm an}^2 - \omega_{\rm SOT}^2}. \quad \text{(C6)}$$

For the experiment-related parameters that have been used to analyze the stability of FM state, $A < 1$ and $B < \omega_{\rm an}$. So, we can estimate that the current a_1 and a_2 are all positive. According to the Routh-Hurwitz Criterion [77–79], the real parts of all roots of λ are negative, and these two tilted-AFM states are stable. In addition, the solutions of θ^0 and ϕ^0 must be real. Then, from Eq. (14), one has $|\omega_{\rm SOT}| < \omega_{\rm an}$. This inequation can be regarded as a linear stability condition.

For $P = 2$ and 4, a_1 is the same as Eq. (C3),

$$a_2 = -2\frac{AB(3\omega_{\rm ex} + \omega_{\rm an} + B)}{(1 + \beta^2)\beta^2\omega_{\rm SOT}^2}\Big\{[(3\omega_{\rm ex} + \omega_{\rm an}) - (1 + \beta^2)B]^2 + \beta^2\big[(3\omega_{\rm ex} + \omega_{\rm an})^2 - (1 + \beta^2)\omega_{\rm an}^2\big]\Big\}. \quad \text{(C7)}$$

Obviously, $a_2 < 0$ for the realistic experimental situation. Thus, these two tilted-AFM states are unstable.

[1] E. V. Gomonay and V. M. Loktev, Low Temp. Phys. **40**, 17 (2014).
[2] T. Jungwirth, X. Marti, P. Wadley, and J. Wunderlich, Nat. Nanotechnol. **11**, 231 (2016).
[3] V. Baltz, A. Manchon, M. Tsoi, T. Moriyama, T. Ono, and Y. Tserkovnyak, Rev. Mod. Phys. **90**, 015005 (2018).
[4] E. G. Tveten, A. Qaiumzadeh, and A. Brataas, Phys. Rev. Lett. **112**, 147204 (2014).
[5] S. K. Kim, Y. Tserkovnyak, O. Tchernyshyov, Phys. Rev. B **90**, 104406 (2014).
[6] S. M. Rezende, A. Azevedo, and R. L. Rodríguez-Suárez, J. Appl. Phys. **126**, 151101 (2019).
[7] A. Manchon, J. Železný, I. M. Miron, T. Jungwirth, J. Sinova, A. Thiaville, K. Garello, and P. Gambardella, Rev. Mod. Phys. **91**, 035004 (2019).
[8] K. M. D. Hals, Y. Tserkovnyak, and A. Brataas, Phys. Rev. Lett. **106**, 107206 (2011).
[9] O. Gomonay, T. Jungwirth, and J. Sinova, Phys. Rev. Lett. **117**, 017202 (2016).
[10] T. Shiino, S. H. Oh, P. M. Haney, S. W. Lee, G. Go, B. G. Park, and K. J. Lee, Phys. Rev. Lett. **117**, 087203 (2016).
[11] Y. C. Liang, P. B. He, M. Q. Cai, and Z. D. Li, Jour. Magn. Magn. Mater. **479**, 291 (2019).
[12] P. Wadley, S. Reimers, M. J. Grzybowski, C. Andrews, M. Wang, J. S. Chauhan, B. L. Gallagher, R. P. Campion, K. W. Edmonds, S. S. Dhesi, F. Maccherozzi, V. Novak, J. Wunderlich, and T. Jungwirth, Nat. Nanotechnol. **13**, 362 (2018).
[13] H. V. Gomonay and V. M. Loktev, Phys. Rev. B **81**, 144427 (2010).
[14] J. Linder, Phys. Rev. B **84**, 094404 (2011).
[15] R. Cheng, M. W. Daniels, J.-G. Zhu, and D. Xiao, Phys. Rev. B **91**, 064423 (2015).
[16] P. Wadley, B. Howells, J. Železný, C. Andrews, V. Hills, R. P. Campion, V. Novák, K. Olejník, F. Maccherozzi, S. S. Dhesi, S. Y. Martin, T. Wagner, J. Wunderlich, F. Freimuth, Y. Mokrousov, J. Kuneš, J. S. Chauhan, M. J. Grzybowski, A. W. Rushforth, K. W. Edmonds, B. L. Gallagher, and T. Jungwirth, Science **351**, 587 (2016).
[17] X. Z. Chen, R. Zarzuela, J. Zhang, C. Song, X. F. Zhou, G. Y. Shi, F. Li, H. A. Zhou, W. J. Jiang, F. Pan, and Y. Tserkovnyak, Phys. Rev. Lett. **120**, 207204 (2018).
[18] C. C. Chiang, S. Y. Huang, D. Qu, P. H. Wu, and C. L. Chien, Phys. Rev. Lett. **123**, 227203 (2019).
[19] R. Cheng, D. Xiao, and A. Brataas, Phys. Rev. Lett. **116**, 207603 (2016).
[20] R. Khymyn, I. Lisenkov, V. Tiberkevich, B. A. Ivanov, and A. Slavin, Sci. Rep. **7**, 43705 (2017).
[21] R. E. Troncoso, K. Rode, P. Stamenov, J. M. D. Coey, and A. Brataas, Phys. Rev. B **99**, 054433 (2019).
[22] D.-K. Lee, B.-G. Park, and K.-J. Lee, Phys. Rev. Appl. **11**, 054048 (2019).

[23] H. Chen, Q. Niu, and A. H. MacDonald, Phys. Rev. Lett. **112**, 017205 (2014).

[24] X. Zhou, J.-P. Hanke, W. Feng, F. Li, G.-Y. Guo, Y. Yao, S. Blügel, and Y. Mokrousov, Phys. Rev. B **99**, 104428 (2019).

[25] K. Zhao, T. Hajiri, H. Chen, R. Miki, H. Asano, and P. Gegenwart, Phys. Rev. B **100**, 045109 (2019).

[26] V. T. N. Huyen, M.-T. Suzuki, K. Yamauchi, and T. Oguchi, Phys. Rev. B **100**, 094426 (2019).

[27] G. Gurung, D.-F. Shao, T. R. Paudel, and E. Y. Tsymbal, Phys. Rev. Materials **3**, 044409 (2019).

[28] D. Boldrin, I. Samathrakis, J. Zemen, A. Mihai, B. Zou, F. Johnson, B. D. Esser, D. W. McComb, P. K. Petrov, H. Zhang, and L. F. Cohen, Phys. Rev. Materials **3**, 094409 (2019).

[29] I. Samathrakis and H. Zhang, Phys. Rev. B **101**, 214423 (2020).

[30] Y. You, H. Bai, X. Chen, Y. Zhou, X. Zhou, F. Pan, and C. Song, Appl. Phys. Lett. **117**, 222404 (2020).

[31] J. Kübler and C. Felser, Europhys. Lett. **108**, 67001 (2014).

[32] S. Nakatsuji, N. Kiyohara, and T. Higo, Nature (London) **527**, 212 (2015).

[33] N. Kiyohara, T. Tomita, and S. Nakatsuji, Phys. Rev. Appl. **5**, 064009 (2016).

[34] A. K. Nayak, J. E. Fischer, Y. Sun, B. Yan, J. Karel, A. C. Komarek, C. Shekhar, N. Kumar, W. Schnelle, J. Kübler, C. Felser, and S. P. P. Parkin, Sci. Adv. **2**, e1501870 (2016).

[35] Y. Zhang, Y. Sun, H. Yang, J. Železný, S. P. P. Parkin, C. Felser, and B. Yan, Phys. Rev. B **95**, 075128 (2017).

[36] T. Higo, D. Qu, Yufan Li, C. L. Chien, Y. Otani, and S. Nakatsuji, Appl. Phys. Lett. **113**, 202402 (2018).

[37] H. Bai, W. Zhu, Y. You, X. Chen, X. Zhou, F. Pan, and C. Song, Appl. Phys. Lett. **117**, 052404 (2020).

[38] C. Ulloa and A. S. Nunez, Phys. Rev. B **93**, 134429 (2016).

[39] Y. Yamane, O. Gomonay, and J. Sinova, Phys. Rev. B **100**, 054415 (2019).

[40] S. Sugimoto, Y. Nakatani, Y. Yamane, M. Ikhlas, K. Kondou, M. Kimata, T. Tomita, S. Nakatsuji, and Y. Otani, Commun. Phys. **3**, 111 (2020).

[41] O. V. Gomonay and V. M. Loktev, Low Temp. Phys. **41**, 698 (2015).

[42] H. Fujita, Phys. Status Solidi RRL **11**, 1600360 (2017).

[43] T. Hajiri, S. Ishino, K. Matsuura, and H. Asano, Appl. Phys. Lett. **115**, 052403 (2019).

[44] G. Gurung, D.-F. Shao, and E. Y. Tsymbal, Phys. Rev. B **101**, 140405(R) (2020).

[45] Y. Takeuchi, Y. Yamane, J.-Y. Yoon, R. Itoh, B. Jinnai, S. Kanai, J. Ieda, S. Fukami, and H. Ohno, Nat. Mater. **20**, 1364 (2021).

[46] M. Mochizuki, M. Kobayashi, R. Okabe, and D. Yamamoto, Phys. Rev. B **97**, 060401(R) (2018).

[47] L. Perko, *Differential Equations and Dynamical Systems* (Springer, Berlin, 1996), pp. 415–431.

[48] C. Serpicoa, M. D'Aquino, G. Bertotti, and I. D. Mayergoyz, J. Appl. Phys. **95**, 7052 (2004).

[49] G. Bertotti, C. Serpico, I. D. Mayergoyz, A. Magni, M. dAquino, and R. Bonin, Phys. Rev. Lett. **94**, 127206 (2005).

[50] C. Serpico, M. D'Aquino, G. Bertotti, and I. D. Mayergoyz, Jour. Magn. Magn. Mater. **290-291**, 502 (2005).

[51] G. Bertotti, I. D. Mayergoyz, and C. Serpico, *Nonlinear Magnetization Dynamics in Nanosystems* (Elsevier, Amsterdam, 2009), pp. 242–260.

[52] M. D. Stiles and J. Miltat, *Spin Dynamics in Confined Magnetic Structures III*, edited by B. Hillebrands and A. Thiaville (Springer, New York, 2006), pp. 269–274, 295–300.

[53] T. Taniguchi, H. Arai, S. Tsunegi, S. Tamaru, H. Kubota, and H. Imamura, Appl. Phys. Expr. **6**, 123003 (2013).

[54] T. Taniguchi, H. Arai, H. Kubota, and H. Imamura, IEEE Trans. Magn. **50**, 1400404 (2014).

[55] T. Taniguchi, S. Tsunegi, H. Kubota, and H. Imamura, Appl. Phys. Lett. **104**, 152411 (2014).

[56] T. Taniguchi, S. Tsunegi, H. Kubota, and H. Imamura, J. Appl. Phys. **117**, 17C504 (2015).

[57] T. Taniguchi, T. Ito, Y. Utsumi, S. Tsunegi, and H. Kubota, J. Appl. Phys. **118**, 053903 (2015).

[58] T. Taniguchi, Phys. Rev. B **91**, 104406 (2015).

[59] T. Taniguchi and H. Kubota, Phys. Rev. B **93**, 174401 (2016).

[60] T. Taniguchi, T. Ito, S. Tsunegi, H. Kubota, and Y. Utsumi, Phys. Rev. B **96**, 024406 (2017).

[61] U. Ebels, D. Houssameddine, I. Firastrau, D. Gusakova, C. Thirion, B. Dieny, and L. D. Buda-Prejbeanu, Phys. Rev. B **78**, 024436 (2008).

[62] D. Pinna, A. D. Kent, and D. L. Stein, Phys. Rev. B **88**, 104405 (2013).

[63] D. Pinna, D. L. Stein, and A. D. Kent, Phys. Rev. B **90**, 174405 (2014).

[64] K. A. Newhall and E. Vanden-Eijnden, J. Appl. Phys. **113**, 184105 (2013).

[65] T. Taniguchi, Y. Utsumi, M. Marthaler, D. S. Golubev, and H. Imamura, Phys. Rev. B **87**, 054406 (2013).

[66] W. H. Butler, T. Mewes, C. K. A. Mewes, P. B. Visscher, William H. Rippard, S. E. Russek, and R. Heindl, IEEE Trans. Magn. **48**, 4684 (2012).

[67] Q. H. Li, P. B. He, M. Q. Cai, and Z. D. Li, New J. Phys. **23**, 113020 (2021).

[68] Lijun Zhu, D. C. Ralph, and R. A. Buhrman, Phys. Rev. Appl. **10**, 031001(R) (2018).

[69] C.-F. Pai, Y. Ou, L. H. Vilela-Leão, D. C. Ralph, and R. A. Buhrman, Phys. Rev. B **92**, 064426 (2015).

[70] Z. L. Wang, H. Y. Cheng, K. W. Shi, Y. Liu, J. F. Qiao, D. Q. Zhu, W. L. Cai, X. Y. Zhang, S. Eimer, D. P. Zhu, J. Zhang, A. Fert, and W. S. Zhao, Nanoscale **12**, 15246 (2020).

[71] J. H. Hubbard and B. H. West, *Differential Equations: A Dynamical Systems Approach: Higher-Dimensional Systems.* (Springer, New York, 1995), pp. 162–167.

[72] J. Sun, Physics **1**, 33 (2008).

[73] S. Iihama, T. Taniguchi, K. Yakushiji, A. Fukushima, Y. Shiota, S. Tsunegi, R. Hiramatsu, S. Yuasa, Y. Suzuki, and H. Kubota, Nat. Electron. **1**, 120 (2018).

[74] Seung-heon C. Baek, V. P. Amin, Y.-W. Oh, G. Go, S.-J. Lee, G.-H. Lee, K.-J. Kim, M. D. Stiles, B.-G. Park, and K.-J. Lee, Nat. Mater. **17**, 509 (2018).

[75] A. L. Balk, N. H. Sung, S. M. Thomas, P. F. S. Rosa, R. D. McDonald, J. D. Thompson, E. D. Bauer, F. Ronning, and S. A. Crooker, Appl. Phys. Lett. **114**, 032401 (2019).

[76] X. F. Han, X. Wang, C. H. Wan, G. Q. Yu, and X. R. Lv, Appl. Phys. Lett. **118**, 120502 (2021).

[77] E. J. Routh, *A Treatise on the Stability of a Given State of Motion: Particularly Steady Motion* (Macmillan and Co., London, 1877).

[78] A. Hurwitz, Math. Ann. **46**, 273 (1895).

[79] P. Baláž and J. Barnaś, Phys. Rev. B **88**, 014406 (2013).